JOURNAL OF SPACECRAFT AND ROCKETS
Vol. 37, No. 2, March–April 2000

Euler and Navier–Stokes Simulations of Two-Stage Hypersonic Vehicle Longitudinal Motions

Tomislav Cvrlje,* Christian Breitsamter,† Caroline Weishäupl,‡ and Boris Laschka§
Technical University of Munich, 85747 Garching, Germany

The separation maneuver of an idealized two-stage hypersonic vehicle is aerodynamically investigated at a freestream Mach number of 6.8. The focus is on the calculation of unsteady flowfields arising from a pitching and a translatory motion as part of the complete separation maneuver. The numerical simulations are based on a finite volume method for solutions of the two-dimensional unsteady Euler and Navier–Stokes equations. The method is employed to compute the hypersonic flow over a blunt orbital stage including the recirculation zone in the rear of the orbital vehicle. The carrier stage is modeled as a flat plate parallel to the undisturbed flow. The orbital stage, interfering with the carrier, performs a defined motion at zero incidence. The results include the Mach number and pressure distributions, as well as the aerodynamic coefficients. The separation process is dominated by reflecting shock waves occurring during the maneuver between the carrier stage and the orbital stage. The position and intensity of the shock waves are a function of speed, distance, and incidence between the two stages. The main intention is to analyze the motion-induced unsteady aerodynamic effects and the associated flow physics predicted by Euler and Navier–Stokes solutions.

Nomenclature

a_i^ℓ	= ℓth eigenvalue in i direction
c	= speed of sound
c_D	= drag coefficient
c_f	= skin friction coefficient
c_L	= lift coefficient
c_m	= pitch moment coefficient
c_p	= pressure coefficient
$c_{p,\infty}$	= specific heat at constant pressure
e	= density of total energy
$\boldsymbol{F}^I, \boldsymbol{G}^I$	= inviscid flux vectors in curvilinear coordinates
$\boldsymbol{F}^V, \boldsymbol{G}^V$	= viscous flux vectors in curvilinear coordinates
h	= distance between the orbital stage and the carrier stage
J	= Jacobian determinant of grid transformation
k	= reduced frequency, $L\,\omega\sqrt{(\rho_\infty / p_\infty)}/(M_\infty\sqrt{\gamma})$
k	= conductivity
L	= orbital stage reference length, ramp reference length
$\boldsymbol{L}$	= matrix of the left eigenvectors, $\boldsymbol{R}^{-1}$
M	= Mach number
P, Q	= source strengths
Pr	= Prandtl number, $c_{p,\infty}\,\mu_\infty / k_\infty$
p	= pressure
$\boldsymbol{R}$	= matrix of the right eigenvectors
Re	= Reynolds number, $\rho_\infty U_\infty L/\mu_\infty$
t	= time
$\boldsymbol{U}$	= vector of conservative variables
U, V	= contravariant velocities
U_∞	= freestream velocity
u, v	= velocity components in x and y directions
x, y	= Cartesian coordinates
α	= angle of attack, deg
α_i^ℓ	= wave strength
γ	= ratio of specific heat
$\tilde{\delta}$	= parameter of numerical dissipation
μ	= viscosity
ξ, η	= curvilinear coordinates
ρ	= density
τ	= dimensionless time, $M_\infty\sqrt{(\gamma)}\,t\,\sqrt{(p_\infty/\rho_\infty)}/L$
Φ	= nonlinear term of the numerical flux
Ψ	= entropy correction parameter
ω	= angular frequency

Subscripts

W	= wall
∞	= freestream values

Received 15 June 1999; revision received 23 November 1999; accepted for publication 30 November 1999.

*Research Engineer, Lehrstuhl für Fluidmechanik. Member AIAA.
†Chief Engineer, Lehrstuhl für Fluidmechanik. Member AIAA.
‡Scientific Engineer, Lehrstuhl für Fluidmechanik. Member AIAA.
§Full Professor, Fluid Mechanics, Lehrstuhl für Fluidmechanik. Honorary Fellow AIAA.

Introduction

THE demands for new space transportation systems have increased-research efforts on hypersonic technology worldwide.[1–3] In the last few years hypersonic research activities were pushed by the development of hypersonic vehicle demonstrators, for example, within the NASA Hyper-X Program and the X-33 Reusable Launch Vehicle Demonstrator Program.[4] The European and national projects concentrate mainly on system studies and fundamental research activities, for example, within the German Hypersonics Technology Program,[5] the Future European Space Transportation Investigations Program (FESTIP), and the Technologies for Future Space Transportation Systems (TETRA).[6] Although these programs have broadened the knowledge in the field of hypersonic research, there are still a lot of challenging problems in many technological areas. Hence, a significant need for fundamental hypersonic research exists.

In particular, comprehensive investigations dealing with the key technologies for a two-stage space transportation system are performed at the Technical University of Munich. This concept of a fully reusable hypersonic vehicle deals with a delta-winged first stage powered by airbreathing engines. It is launched horizontally with the orbital stage mounted bottom-to-top. At high altitude (35 km) and high Mach number ($M_\infty = 6.8$) the orbital stage is released and the separation phase starts. Experience concerning the separation of lifting vehicles has been mainly gathered for the subsonic velocity regime,[7] whereas for the separation of hypersonic vehicles only limited investigations have been conducted.[8] The separation maneuver at supersonic speed reveals some serious problems. Consequently, there is a need to describe and to analyze the separation process at high Mach numbers to provide fundamental knowledge on unsteady aerothermodynamics.

The separation phase is mainly dominated by aerodynamic interference effects. For interfering bodies, several measurements and calculations have been performed during the Space Shuttle

program dealing with the separation of the liquid-fuel tank from the orbiter.[9] However, all investigations assume a steady flowfield and, thus, neglect additional velocities induced from the separation maneuver.[10,11] Numerical simulations involving both roll and yaw oscillations of an orbital vehicle for different reduced frequencies indicate that the unsteady effects are not negligible.[12–14] Furthermore, the unsteady calculations show that during the separation process strong reflecting shock waves are propagated downstream from the nose of the orbital stage. The shock waves are reflected from the carrier vehicle and strike again the lower side of the orbital vehicle.[15,16] As the separation distance between the orbital stage and the carrier stage alters, the points of intersection of the reflected shock waves change as well. This alteration of the intersection points causes strong unsteady airloads on the orbital stage and, to a lesser extent, on the carrier stage. These investigations were based on the solution of the Euler equations.[15,16] Therefore, features of the separation process due to friction effects have not been considered. Consequently, this paper deals with Euler and Navier–Stokes calculations investigating the unsteady effects associated with the separation of hypersonic vehicles. Main flow features such as bow shock and reflected shock waves between the vehicles are predicted similarily by both methods. In addition, the Navier–Stokes solutions show motion-dependent areas of separated flow occurring on the lower side of the orbital stage affecting the local flowfield between the stages as well as the airloads.

Geometry and Grid Generation

Geometry of Orbital Stage

The calculations are conducted for an idealized orbital stage interfering with a flat plate representing the carrier stage. Figure 1 presents the geometry of the orbital vehicle and the carrier. The orbital stage contour is modeled by two partial ellipses, a mainly flat lower side and a flat base. The contour of the body is described from a set of 180 points using an algebraic grid generator.

Method of Grid Generation

A multiblock segmentation of the calculated domain is introduced to provide structured meshes for general shaped bodies. The construction of block topology is based on that only one boundary condition type can be applied to any block face. Therefore, the administration expenditure is reduced within both the grid generator and the Navier–Stokes solver. To generate the initial grid, a transfinite interpolation is employed. The subsequential use of a Poisson algorithm results in smoothing out the initial grid and, thus, guarantees small cell deformations and continuous cell growth. The grid algorithm is based on solving the system of Poisson equations[17]:

$$g_{22}(\boldsymbol{r}_{\xi\xi} + P\boldsymbol{r}_{\xi}) + g_{11}(\boldsymbol{r}_{\eta\eta} + Q\boldsymbol{r}_{\eta}) - 2g_{12}\boldsymbol{r}_{\xi\eta} = 0 \qquad (1)$$

with $\boldsymbol{r} = [x, y]^T$ and the covariant metric coefficients g_{ij}. The source terms P and Q are responsible for the motion of the grid lines in the corresponding positive or negative coordinate direction during the iteration loop and, thus, provide the control of grid point spacing and distribution. To guarantee orthogonality, the mixed metric coefficients g_{12} are set to zero. After the generation of an analytical grid, the source terms are determined at the solid body by inverting the Poisson equation. Mirror points with a fixed distance from the solid body wall are employed to calculate the symmetric derivatives at block boundaries. The Laplace equation is used to spread the source terms into the calculation domain.

The described procedure of elliptic smoothing is applied for each block and, in the same manner, over block boundaries. The connections between adjacent blocks are organized by mother-child relations, where the grid points located at block connections are allowed to move during the iteration process.[18] The convergence criterion for sufficient smoothness is fullfilled if the change in the source strengths is below 10^{-5}.

Unsteady calculations are performed by adapting the grid dynamically to the actual body position. The separating body is moved for each time step with respect to the prescribed motion. Because of the motion-induced mesh deformations near the body, it is necessary to smooth the grid again using the Poisson algorithm. The velocity of the mesh and the deformation of the cells are considered in the unsteady transformation of the Euler and Navier–Stokes equations, respectively.

The just method explained presents a stable and flexible tool to generate grids for steady and unsteady applications. Cell singularities or overlaps are avoided. The distribution of points is performed to represent adequately the geometrical shape of the body and to concentrate them in regimes with high gradients of both the body contour and the flow variables.

Computational Mesh

The computational domain employs six blocks arranged in a hybrid C–H topology (Fig. 2). The grid consists of 9000 cells for both Euler and Navier–Stokes calculations. For the inviscid case, the distance of the first off-body grid line is fixed at $3 \times 10^{-3} L$. For the viscous case, this distance is reduced to $3 \times 10^{-4} L$ resulting in a sufficient spatial resolution of the orbital stage boundary layer with about five cells at $x/L = 0.5$.

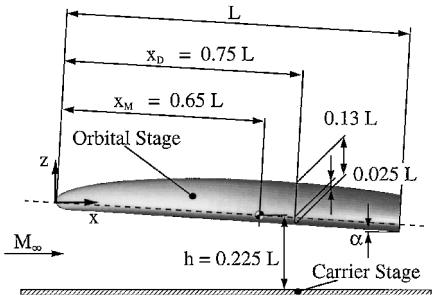

Fig. 1 Geometry of the generic orbital stage.

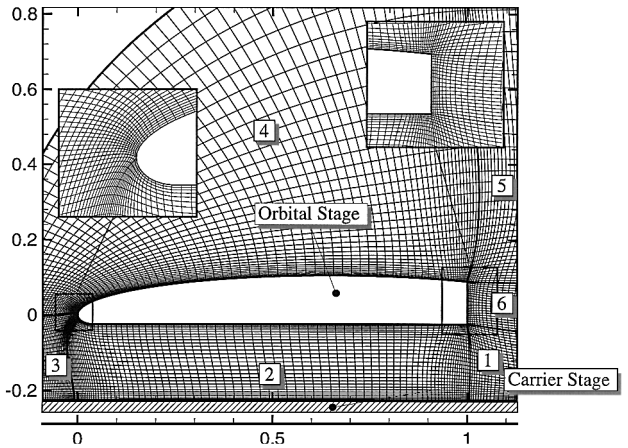

Mesh for Euler calculations

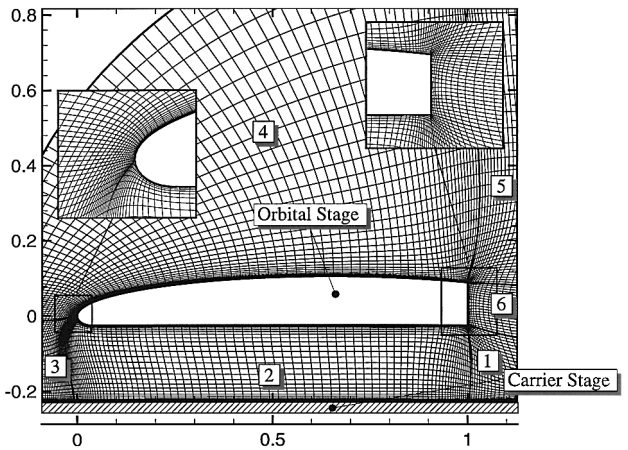

Mesh for Navier–Stokes calculations

Fig. 2 Computational mesh with C–H topology using 9000 cells arranged in six blocks.

Numerical Method

Governing Equations

The algorithm to solve the unsteady Navier–Stokes equations is based on a finite volume approximation to the integral form of the governing conservation laws. The conservation form of the two-dimensional Navier–Stokes equations in curvilinear coordinates can be written as[19]

$$\frac{\partial \boldsymbol{U}}{\partial \tau} + \frac{\partial \boldsymbol{F}}{\partial \xi} + \frac{\partial \boldsymbol{G}}{\partial \eta} = 0 \tag{2}$$

with the flux vectors

$$\boldsymbol{F} = \bar{\boldsymbol{F}}^I - Re_\infty^{-1}\bar{\boldsymbol{F}}^V, \qquad \boldsymbol{G} = \bar{\boldsymbol{G}}^I - Re_\infty^{-1}\bar{\boldsymbol{G}}^V \tag{3}$$

and the dependent variable vector $\boldsymbol{U} = J^{-1}(\rho, \rho u, \rho v, e)^T$. $\bar{\boldsymbol{F}}^I$ and $\bar{\boldsymbol{G}}^I$ denote the inviscid fluxes

$$\bar{\boldsymbol{F}}^I = J^{-1}\begin{bmatrix} \rho U \\ \rho u U + \xi_x p \\ \rho v U + \xi_y p \\ U(e+p) - \xi_t p \end{bmatrix}, \qquad \bar{\boldsymbol{G}}^I = J^{-1}\begin{bmatrix} \rho V \\ \rho u V + \eta_x p \\ \rho v V + \eta_y p \\ V(e+p) - \eta_t p \end{bmatrix}$$

with the contravariant velocities

$$U = \xi_x u + \xi_y v + \xi_t, \qquad V = \eta_x u + \eta_y v + \eta_t \tag{4}$$

J is the Jacobian of the transformation defined with

$$J^{-1} = x_\xi y_\eta - y_\xi x_\eta \tag{5}$$

The metric coefficients are

$$\xi_x = J y_\eta, \qquad \eta_x = -J y_\xi, \qquad \xi_y = -J x_\eta, \qquad \eta_y = J x_\xi \tag{6}$$

and the cell-face velocities ξ_t and η_t are

$$\xi_t = -(x_\tau \xi_x + y_\tau \xi_y), \qquad \eta_t = -(x_\tau \eta_x + y_\tau \eta_y) \tag{7}$$

describing the deformation of the cells within the computational domain. The viscous flux terms $\bar{\boldsymbol{F}}^V$ and $\bar{\boldsymbol{G}}^V$ are

$$\bar{\boldsymbol{F}}^V = J^{-1}\left(\xi_x \boldsymbol{F}^V + \xi_y \boldsymbol{G}^V\right), \qquad \bar{\boldsymbol{G}}^V = J^{-1}\left(\eta_x \boldsymbol{F}^V + \eta_y \boldsymbol{G}^V\right) \tag{8}$$

with

$$\boldsymbol{F}^V = \begin{bmatrix} 0 \\ \tau_{xx} \\ \tau_{xy} \\ u\tau_{xx} + v\tau_{xy} - q_x \end{bmatrix}, \qquad \boldsymbol{G}^V = \begin{bmatrix} 0 \\ \tau_{xy} \\ \tau_{yy} \\ u\tau_{xy} + v\tau_{yy} - q_y \end{bmatrix}$$

Assuming Stokes hypothesis, the components of the viscous stress terms τ_{xx}, τ_{xy}, and τ_{yy} are given by the expressions

$$\tau_{xx} = \frac{2}{3}\mu\left(2\frac{\partial u}{\partial x} - \frac{\partial v}{\partial y}\right), \qquad \tau_{yy} = \frac{2}{3}\mu\left(2\frac{\partial v}{\partial y} - \frac{\partial u}{\partial x}\right)$$

$$\tau_{xy} = \mu\left(\frac{\partial u}{\partial y} + \frac{\partial v}{\partial x}\right) = \tau_{xy} \tag{9}$$

where μ is the coefficient of viscosity. The components of the heat fluxes are

$$q_x = -\frac{\mu}{M^2(\gamma-1)Pr}\frac{\partial T}{\partial x}, \qquad q_y = -\frac{\mu}{M^2(\gamma-1)Pr}\frac{\partial T}{\partial y} \tag{10}$$

considering a constant Prandtl number leading to $k = \mu$ for nondimensional values. The viscosity coefficient μ is determined by the Sutherland law:

$$\mu = T^{\frac{3}{2}}[(1+C)/(T+C)] \tag{11}$$

where $C = 110.4/T_\infty$ for air.[19]

Numerical Solution

The calculation of the dependent vector $\boldsymbol{U}$ is performed by means of a finite volume approximation to Eq. (2) using an explicit time integration. Associating the subscripts k and l with the ξ and η directions, the numerical approximation may be expressed in a discrete conservation law form given by

$$\frac{\Delta \tilde{U}_{k,1}}{\Delta \tau} = -\frac{1}{\Delta \xi}\left(\tilde{\boldsymbol{F}}^n_{k+\frac{1}{2},l} - \tilde{\boldsymbol{F}}^n_{k-\frac{1}{2},l}\right) - \frac{1}{\Delta \eta}\left(\tilde{\boldsymbol{G}}^n_{k,l+\frac{1}{2}} - \tilde{\boldsymbol{G}}^n_{k,l-\frac{1}{2}}\right) \tag{12}$$

where

$$\tilde{\boldsymbol{F}} = \tilde{\boldsymbol{F}}^I - Re_\infty^{-1}\tilde{\boldsymbol{F}}^V, \qquad \tilde{\boldsymbol{G}} = \tilde{\boldsymbol{G}}^I - Re_\infty^{-1}\tilde{\boldsymbol{G}}^V$$

denote the numerical fluxes at the bounding sides of the cell k and l in the ξ and η directions. $\tilde{\boldsymbol{U}}_{k,l}$ is the conservative quantity that represents the numerical approximation to $\boldsymbol{U}$ and is considered to be the centroidal value. The calculation of the dependent vector is based on the assumption that the fluxes normal to cell faces are independent from the parallel ones. Thus, the two-dimensional Navier–Stokes equations can be split into one-dimensional equations, which are solved independently. The total change of the dependent vector is determined by linear superposition of the parts in both directions.

Total Variation Diminishing Discretization of the Inviscid Flux Vector

The inviscid fluxes $\tilde{\boldsymbol{F}}^I$ and $\tilde{\boldsymbol{G}}^I$ are calculated by the method of Yee et al.[20] Flux-limiting functions are introduced to guarantee the spatial second-order accuracy in smooth regions as well as the total variation diminishing (TVD) character of the solver. To evaluate the numerical flux, we concentrate on $\tilde{\boldsymbol{F}}^I_{k+1/2}$ at the cell face $(k+\frac{1}{2})$ between the cells $(k+1)$ and k:

$$\tilde{\boldsymbol{F}}^I_{k+\frac{1}{2}} = \frac{1}{2}\left(\tilde{\mathbf{F}}^I_k + \tilde{\mathbf{F}}^I_{k+1} + \boldsymbol{R}_{k+\frac{1}{2}}\Phi_{k+\frac{1}{2}}\right) \tag{13}$$

where $\boldsymbol{R}_{k+1/2}$ is the matrix of the right eigenvectors. The components of the eigenvector are determined using the averaging procedure of Chakravarthy and Osher[21] for the interface values of density ρ, velocities, and enthalpy $H = (e+p)/\rho$:

$$\Omega_{k+\frac{1}{2}} = \frac{\Omega_k + D\,\Omega_{k+1}}{1+D} \qquad \text{with} \qquad D = \sqrt{\frac{\rho_{k+1}}{\rho_k}}$$

$$\Omega = \rho, u, v, H \tag{14}$$

This averaging leads to slightly higher densities, which have proved advantageous for calculating the wake part of hypersonic blunt-body flows. The vector components $\Phi^\ell_{k+1/2}$ with $(\ell = 1, \ldots, 4)$ can be expressed as

$$\Phi^\ell_{k+\frac{1}{2}} = -\Psi\left(a^\ell_{k+\frac{1}{2}}\right)\left[\alpha^\ell_{k+\frac{1}{2}} - Q^\ell_{k+\frac{1}{2}}\right] \tag{15}$$

where $a_{k+1/2}$ are the eigenvalues of the matrix. The function $Q^\ell_{k+1/2}$ is the limiter providing the second-order accuracy of the scheme. At points of discontinuous change of the state variables, the function vanishes, which results in a switch in accuracy of the method to first order to avoid wiggles. For $Q^\ell_{k+1/2}$, the minmod function is chosen:

$$Q^\ell_{k+\frac{1}{2}} = 2\,\text{minmod}\left(\alpha^\ell_{k-\frac{1}{2}}, \alpha^\ell_{k+\frac{1}{2}}, \alpha^\ell_{k+\frac{3}{2}}, \frac{1}{4}\left(\alpha^\ell_{k-\frac{1}{2}} + \alpha^\ell_{k+\frac{3}{2}}\right)\right) \tag{16}$$

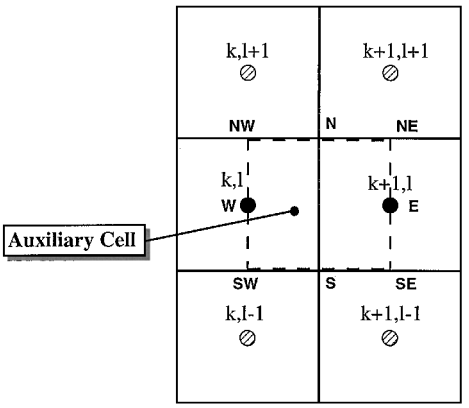

Fig. 3 Cells for viscous calculation.

The wave strengths are given by

$$\alpha^{\ell}_{k+\frac{1}{2}} = \boldsymbol{R}^{-1}_{k+\frac{1}{2}}(\tilde{\boldsymbol{U}}_{k+1} - \tilde{\boldsymbol{U}}_k) \tag{17}$$

The function Ψ is the entropy correction function to $|z|$, designed to exclude nonphysical solutions of expansion shocks:

$$\Psi(z) = \begin{cases} |z|, & |z| \geq \delta \\ \dfrac{z^2 + \delta^2}{2\delta}, & |z| < \delta \end{cases} \tag{18}$$

The parameter δ is calulated as the product of an empirical determined constant δ_1 and the maximum speed at the corresponding cell interface:

$$\delta = \delta_1 (|\Theta_i| + c\,|\nabla k|) \qquad \text{for} \qquad i = k, l \tag{19}$$

with $\Theta = k_x u + k_y v + k_t$ and $|\nabla k| = \sqrt{(k_x^2 + k_y^2)}$ for $k = \xi, \eta$.

Discretization of the Viscous Flux Vector

The viscous fluxes $\tilde{\boldsymbol{F}}^V$ and $\tilde{\boldsymbol{G}}^V$ are calculated according to Chakravarthy.[22] To evaluate the numerical flux at the cell face $(i + \frac{1}{2})$ between the cells $(i + 1)$ and i with $i = k, l$, an auxiliary cell is introduced (Fig. 3) to determine the derivative terms Ω_x and Ω_y with $\Omega = u, v, T$. The corners of the cell are denoted by NW, SW, SE, and NE, and the approximate midpoints of the sides are given as N, W, S, and E. The x and y coordinates of the auxiliary cell are computed by interpolation from the vertices of the original cells. If it is assumed that the values u, v, and T related to the points N, W, S, and E are constant along the respective sides, the derivatives of the values are obtained by using the Gauss integral formula applied to the auxiliary cell A_{aux}. Hence, the derivatives of Ω with $\Omega = u, v, T$ for the cell face $(k + \frac{1}{2})$ are given by

$$\begin{aligned} (\Omega_x)_{k+\frac{1}{2}} &\approx (1/A_{\text{aux}})[\Omega_E\,\mathrm{d}y_E + \Omega_N\,\mathrm{d}y_N + \Omega_W\,\mathrm{d}y_W + \Omega_S\,\mathrm{d}y_S] \\ (\Omega_y)_{k+\frac{1}{2}} &\approx -(1/A_{\text{aux}})[\Omega_E\,\mathrm{d}x_E + \Omega_N\,\mathrm{d}x_N + \Omega_W\,\mathrm{d}x_W + \Omega_S\,\mathrm{d}x_S] \end{aligned} \tag{20}$$

with

$$\mathrm{d}\boldsymbol{r}_E = \boldsymbol{r}_{\text{NE}} - \boldsymbol{r}_{\text{SE}}, \qquad \mathrm{d}\boldsymbol{r}_N = \boldsymbol{r}_{\text{NW}} - \boldsymbol{r}_{\text{NE}}$$

$$\mathrm{d}\boldsymbol{r}_W = \boldsymbol{r}_{\text{SW}} - \boldsymbol{r}_{\text{NW}}, \qquad \mathrm{d}\boldsymbol{r}_S = \boldsymbol{r}_{\text{SE}} - \boldsymbol{r}_{\text{SW}}$$

for $\boldsymbol{r} = [x, y]^T$. The values Ω at W and E are taken to be the values at k and $(k + 1)$, respectively. Refer to Fig. 3; the values Ω_N and Ω_S are defined as

$$\begin{aligned} \Omega_N &\approx \tfrac{1}{4}(\Omega_{k,l} + \Omega_{k,l+1} + \Omega_{k+1,l+1} + \Omega_{k+1,l}) \\ \Omega_S &\approx \tfrac{1}{4}(\Omega_{k,l} + \Omega_{k+1,l} + \Omega_{k+1,l-1} + \Omega_{k,l-1}) \end{aligned} \tag{21}$$

Once all of the derivative terms are evaluated, the stress tensor and heat flux are computed according to Eqs. (9) and (10).

Boundary Conditions

On an impermeable wall, the no-slip conditions for the contravariant velocities have to be fulfilled:

$$U = \xi_x u + \xi_y v + \xi_t = 0, \qquad V = \eta_x u + \eta_y v + \eta_t = 0 \tag{22}$$

The pressure is obtained by the extrapolation from the field value. For hypersonic inflow at the far-field boundary, the flow variables are fixed to their freestream values. The far-field variables for hypersonic outflow are extrapolated by employing the solution in the computational domain.

Complex Representation of the Pressure Variation

To analyze the unsteady effects in detail, the time variation of surface pressures is expressed in terms of Fourier components. The parameter δ associated with the harmonic motion is given by

$$\delta(\tau) = \delta^0 + \mathrm{Re}(\tilde{\delta} e^{ik\tau}) \tag{23}$$

where Re is the real part of the complex argument. The Fourier series of the surface-pressure coefficient for $c_p = C_i$ is

$$C_i(\tau) = C_i^0 + \sum_{j=1}^{n} \mathrm{Re}\left[\tilde{C}_i^j e^{ijk\tau}\right] \tag{24}$$

where C_i^0 is the mean value of the local surface-pressure coefficient and $\tilde{C}_i^j$ is the jth complex component of the local unsteady pressure coefficient. The real and imaginary value of $\tilde{C}_i^j$ can be written as

$$\mathrm{Re}\left[\tilde{C}_i^j\right] = \left|C_i^j\right| \cos\Phi_{ij}, \qquad \mathrm{Im}\left[\tilde{C}_i^j\right] = \left|C_i^j\right| \sin\Phi_{ij} \tag{25}$$

with the magnitude (amplitude) $|C_i^j|$ and the phase shift Φ_{ij} between the motion parameter and the pressure response.

Numerical Accuracy

The accuracy of the Euler code has been proved by calculating several standard test cases for subsonic, supersonic, and hypersonic flow.[13,15,18] Also, the Navier–Stokes code has been validated for a sample of test cases.[13] Typically, Fig. 4 shows the surface pressure and the skin-friction coefficient for hypersonic flow at a 15-deg ramp. The graphs demonstrate that there is quite good agreement between the experimental[23] and numerical[24,25] reference results and the results of the method used herein. In addition, grid refinement studies on the test cases substantiate that the dominant flow features are represented correctly by the grid resolutions used.[13]

Results and Discussion

To investigate the unsteady effects of a complete separation maneuver, both a sinusoidal pitching oscillation and a translatory movement are considered. In both cases, the movement starts from the initial position at $h/L = 0.225$ representing the distance between the carrier stage and the orbital stage at an angle of attack of $\alpha = 0$ deg. The pitching oscillation is performed around the reference moment point at $x/L = 0.65$ and $z/L = 0.025$ with an amplitude of $\Delta\alpha = 2$ deg. The translatory separation is also based on a pitching motion with a center of rotation at $x/L \simeq \infty$ and an amplitude of $\Delta z/L = 0.07$. For all calculations, the freestream Mach number was set to $M_\infty = 6.8$. A reduced frequency of $k = 1.0$ was chosen corresponding to a harmonic oscillation with a frequency of 12.5 Hz based on a reference length of the orbital stage of 27 m. Normal atmospheric conditions are regarded for the separation maneuver taking place at an altitude of 35 km.

Steady Results for the Initial Position

Intensive numerical investigations have shown that during the separation process strong reflecting shock waves occur between

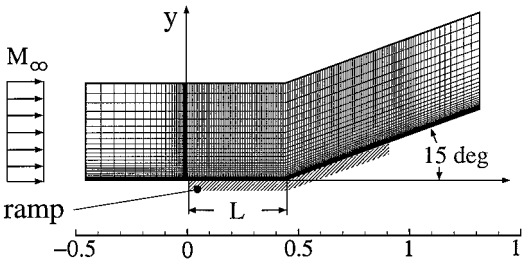

Ramp geometry and computational mesh

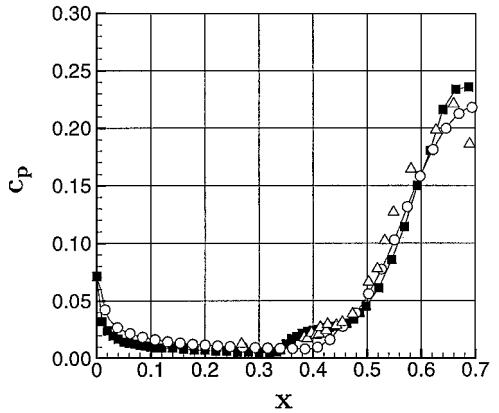

Surface-pressure coefficient

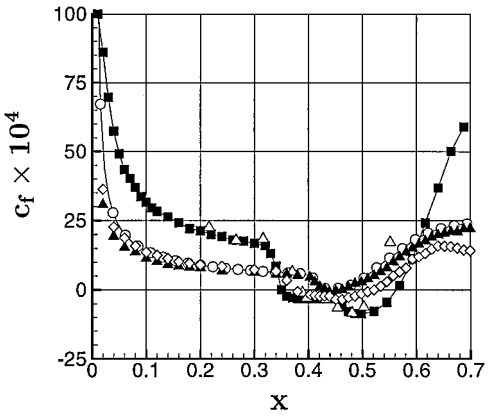

Skin-friction coefficient

Fig. 4 Comparison of surface-pressure and skin-friction coefficients between experimental and numerical reference results and results of the Navier–Stokes method used here for a flow over a 15-deg ramp at $M_\infty = 11.68$, $Re = 2.47 \times 10^5$, $T_\infty = 65.0$ K, and $T_W = 297.0$ K; ○, present explicit TVD method; △, experimental data, Ref. 23; ■, implicit TVD method, Ref. 24; ▲, implicit TVD method, Ref. 25; ◇, explicit Runge–Kutta method, Ref. 25.

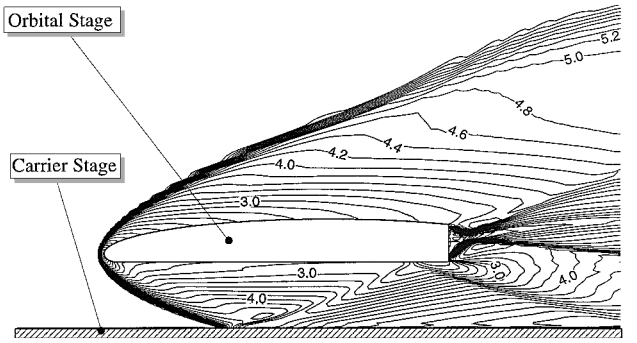

a) Euler calculation

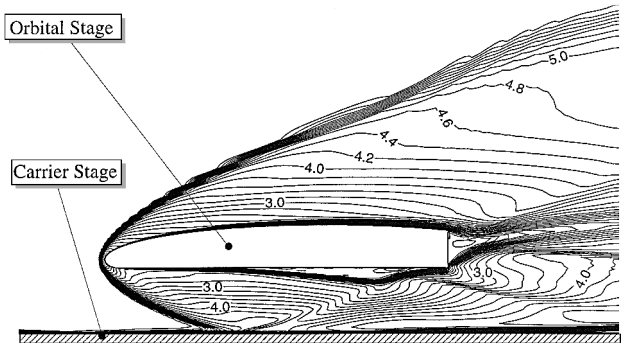

b) Navier–Stokes calculation with $Re = 10^6$

Fig. 5 Mach number contours with $\Delta M/M_\infty = 0.1$ at $M_\infty = 6.8$, $\alpha = 0$ deg, and $h/L = 0.225$.

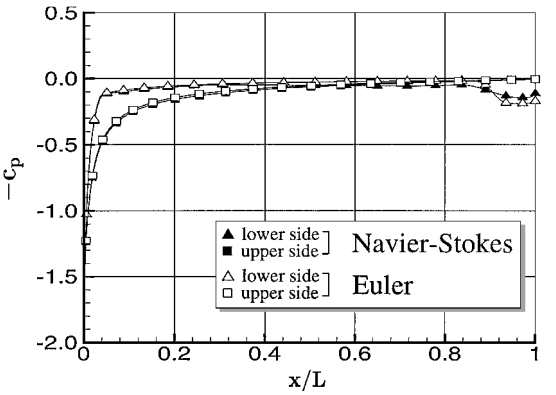

Fig. 6 Steady surface pressure of the orbital stage at $M_\infty = 6.8$, $\alpha = 0$ deg, and $h/L = 0.225$ for Euler and Navier–Stokes calculations ($Re = 10^6$).

the carrier stage and the orbital stage.[16,26] For the initial position ($M_\infty = 6.8$, $h/L = 0.225$, and $\alpha = 0$ deg) the solution of the Euler and Navier–Stokes equations reaches the convergence criterion if the residual of the density is lower than 10^{-6}. The contours of constant Mach numbers are shown in Fig. 5. The flowfields of the entire configuration show basically the same key features for Euler and Navier–Stokes calculations: A bow shock is formed around the blunt nose of the orbital stage. Behind the shock, a strong expansion fan is obvious. The lower part of the shock hits the surface of the carrier stage, where it is reflected. The reflected shock wave strikes again the lower side of the orbital stage. In the wake zone of the orbital stage, a recompression system is formed interfering with the shock wave reflected from the orbital vehicle. Because the pressure on the upper side of the orbital stage is lower than the pressure between both stages, the shock system in the wake region is deflected upwards. The application of the Navier–Stokes equations shows, however, the following differences from the solutions obtained by the Euler calculations. Because of viscous effects, a zone of separated flow occurs on the lower side of the orbital stage.[13] Consequently, in combination with the impinging shock waves, the flowfield differs from the Euler results. The shock wave reflected from the carrier stage does not hit the surface of the orbital stage but strikes the separation zone, where it is reflected again.

From the surface pressure distribution (Fig. 6), the behavior of the shock wave reflection between both stages also can be detected. Euler and Navier–Stokes calculations indicate a local pressure maximum on the lower side of the orbital stage at the shock impinging point. Refer to the Euler results; the shock impinging point is at $x/L \approx 0.90$, whereas the corresponding Navier–Stokes calculations show a slight displacement of the shock downstream to $x/L \approx 0.92$. Considering the Navier–Stokes c_p distribution, the region of separated flow on the lower side of the orbiter starts at $x/L \approx 0.44$, indicated by an area of nearly constant pressure. Because of the absence of any separation bubble, the discontinuity of the pressure coefficient caused by the impinging shock wave is more distinct for the Euler calculation.

Unsteady Results

Pitching Oscillation

For the pitching oscillation, the relatively high reduced frequency of $k = 1.0$ is chosen to study the influence and magnitude of unsteady effects. The motion-induced variation in angle of attack results in a shifting of the shock wave reflection system. The c_p distribution along the orbiter contour arising during the pitching motion downwards is shown in Fig. 7 for several angles of attack. The performed Euler calculations show a movement of the shock impinging point on the lower side of the orbital stage within a range of $0.86 < x/L < 0.95$. For the Navier–Stokes calculations, the movement of the shock impinging point is shifted from $x/L \approx 0.96$ for $\alpha = 1.35$ deg to $x/L \approx 0.90$ for $\alpha = -1.84$ deg. The discontinuity of the pressure coefficient caused by the shock wave reflection is again more distinct for the Euler results. If the Navier–Stokes results are considered, the separation zone on the lower side of the orbital stage results in a nearly constant pressure along the rear part of the vehicle. The c_p distribution for the upper side of the orbital stage is nearly identical for both the Euler and Navier–Stokes calculations.

The harmonic components of the unsteady surface pressure are plotted as real and imaginary parts in Figs. 8 and 9. The modal content of the real part decreases with increasing order of the mode number (Fig. 8). The pressure on the surface ahead of the reflected shock wave is represented mainly by the first harmonic of the Fourier series for both the Euler and Navier–Stokes calculation. In and behind the region of the reflected shock wave on the lower side of the orbital stage, the pressure variations are nonlinear for both calculations. If the associated local maximum of the first harmonic of the Euler results is considered as a reference magnitude, the local maximum of the second harmonic still reaches a level of about 95% and the third harmonic of about 50%. For the Navier–Stokes results, however, a substantially lower local pressure maximum results from the first harmonic, which is about 30% of the corresponding Euler value. With respect to the second and third harmonic of the Navier–Stokes results, the local maxima are ≈86 and ≈43% of the peak value of the first harmonic. Refer to the imaginary parts; both calculations show a strong decreasing tendency with increasing modal number (Fig. 9). Whereas the second harmonic consists of ≈18 and ≈25% of the reference value of the Euler and the Navier–Stokes calculations, respectively, the third mode comprises ≈12 and ≈15%.

The comparison between unsteady Euler and Navier–Stokes airloads at the reduced frequency of $k = 1.0$ is shown in Fig. 10. At the beginning of the motion, the airloads change discontinuously showing periodical tendencies after a quarter-period of motion. A total of four cycles is required to obtain periodical results, although for clarity only the fourth cycle is plotted. Both the moment and

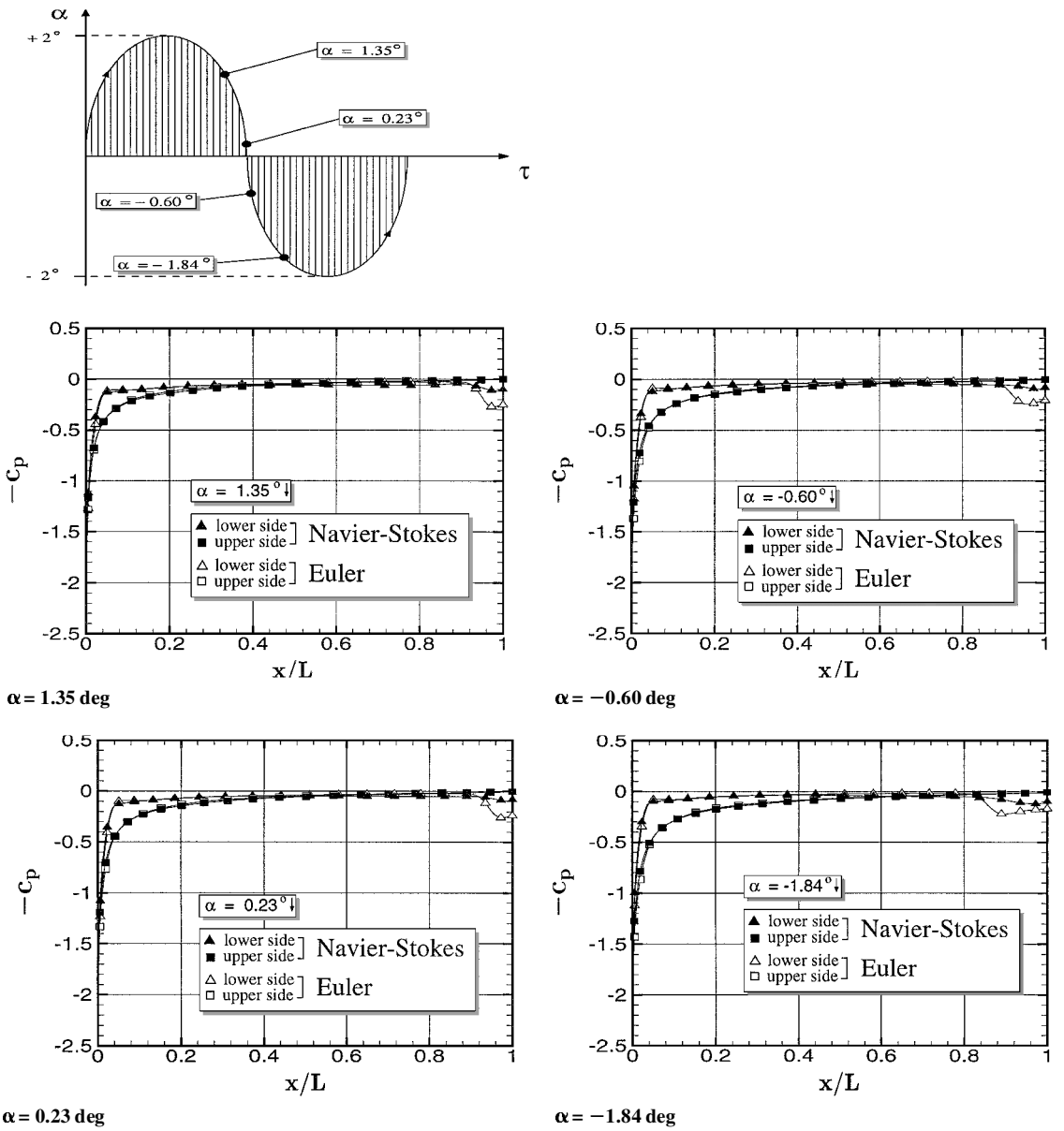

Fig. 7 Orbital stage surface-pressure variation during the pitching oscillation with amplitude $\Delta\alpha = 2$ deg, $k = 1.0$, $M_\infty = 6.8$, $\alpha_0 = 0$ deg, and $h/L = 0.225$ for Euler and Navier–Stokes calculations ($Re = 10^6$).

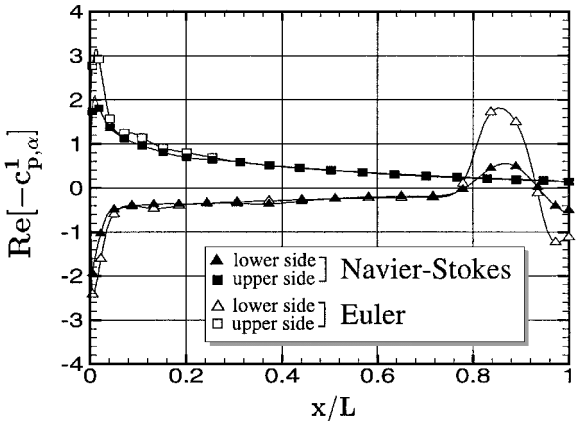

First harmonic

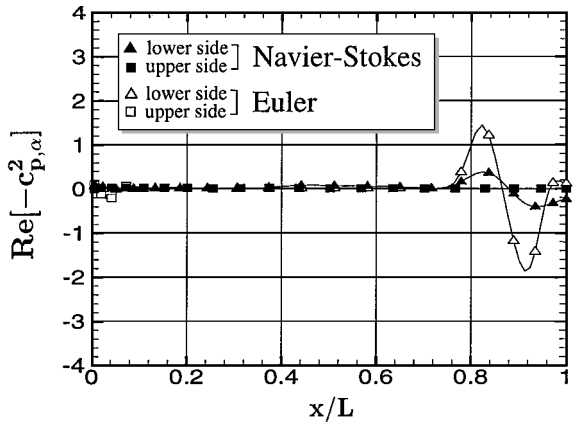

Second harmonic

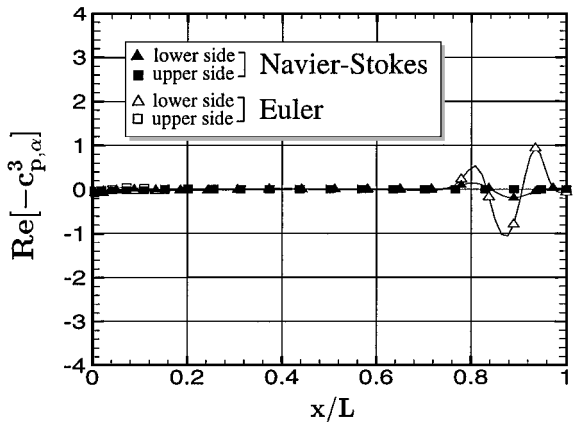

Third harmonic

Fig. 8 Real part of the orbital stage unsteady surface pressure of the pitching oscillation with amplitude $\Delta\alpha = 2$ deg, $k = 1.0$, $M_\infty = 6.8$, $\alpha_0 = 0$ deg, and $h/L = 0.225$ for Euler and Navier–Stokes calculations ($Re = 10^6$).

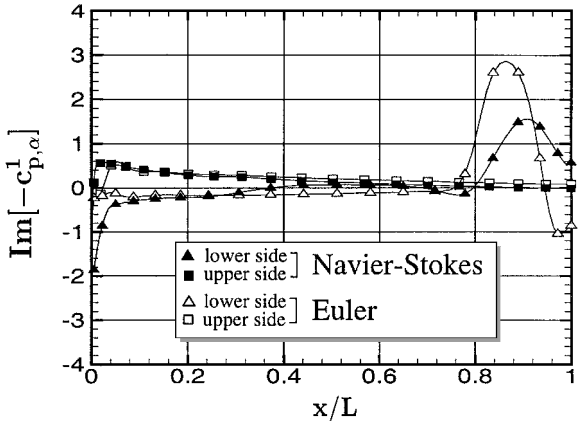

First harmonic

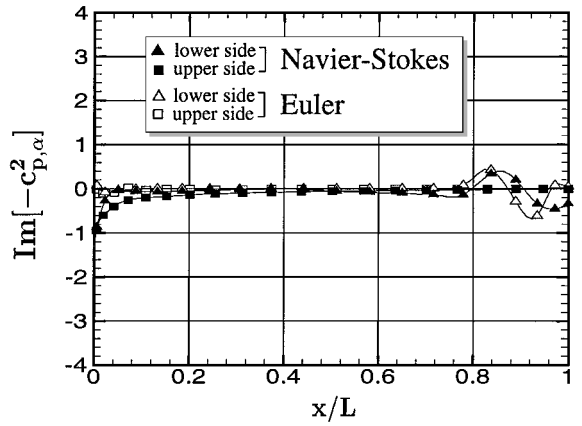

Second harmonic

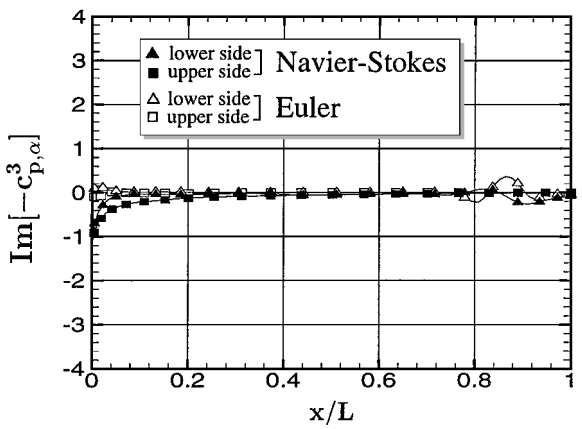

Third harmonic

Fig. 9 Imaginary part of the orbital stage unsteady surface pressure of the pitching oscillation with amplitude $\Delta\alpha = 2$ deg, $k = 1.0$, $M_\infty = 6.8$, $\alpha_0 = 0$ deg, and $h/L = 0.225$ for Euler and Navier–Stokes calculations ($Re = 10^6$).

the lift trajectories follow the counter-clockwise direction. Considering the Navier–Stokes results, the lift coefficient is slightly lower than the Euler results due to the reduced pressure behind the reflected shock wave on the lower side of the orbital stage. The values of the drag coefficient given by the Euler and Navier–Stokes calculations are approximately of the same magnitude. The pressure drag is influenced by the region of very low pressure at the base of the orbital stage. This region is smaller in the inviscid case than in the viscous case. Thus, it may be stated that the expansion system in the wake region of the orbital stage plays an important role for determining the drag coefficient.

Translatory Separation

The orbital vehicle performs the prescribed translatory motion starting from the initial position. For three different vertical positions, that is, $h/L = 0.155$, 0.225, and 0.295, Fig. 11 shows both the contours of Mach number and surface pressure distribution of the orbital stage obtained by the Navier–Stokes calculations. If the closest distance between the orbital stage and the carrier stage ($h/L = 0.155$) is considered, the bow shock reflected from the carrier stage hits the orbital stage at $x/L \approx 0.5$ (Fig. 11a). Compared to Euler calculations,[16] the pressure increases on the lower side of the orbital stage caused by the impinging shock smears over several cells. A separation zone is visible that results in a nearly constant pressure on the lower side of the orbital stage. An increase of the separation distance deflects the shock impinging point in streamwise direction ($x/L \approx 0.65$ for $h/L = 0.225$) (Fig. 11b). At a distance of $h/L = 0.295$, no shock reflection occurs on the lower side of the orbital stage (Fig. 11c). The effect of unsteadiness is clearly obvious for the separation distance at $h/L = 0.225$ for which steady and

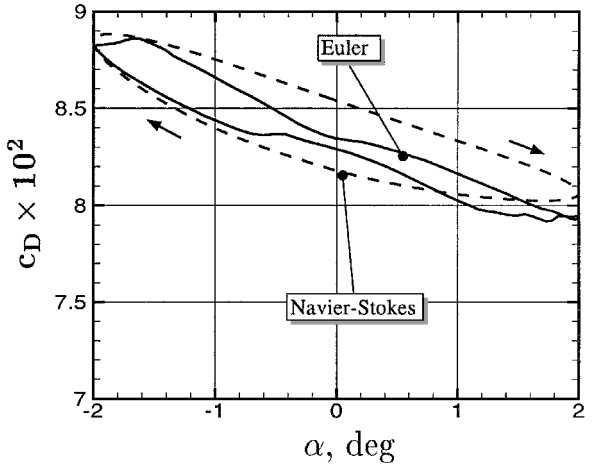

Drag coefficient $c_D(\alpha)$

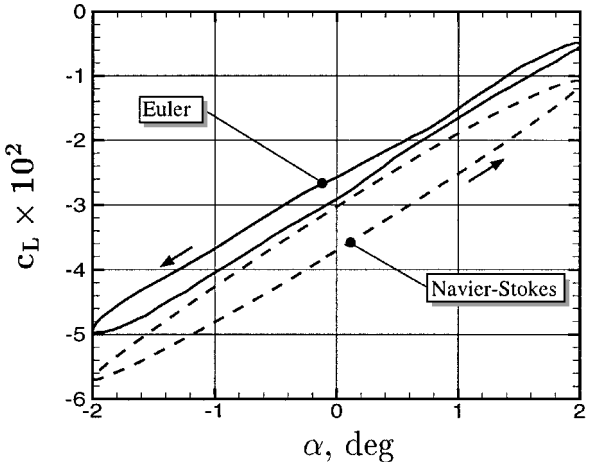

Lift coefficient $c_L(\alpha)$

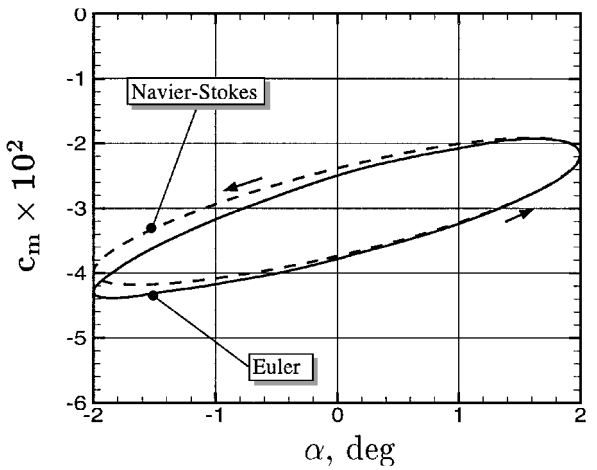

Pitch moment coefficient $c_m(\alpha)$

Fig. 10 Aerodynamic coefficients of the pitching motion of the orbital stage with amplitude $\Delta\alpha = 2$ deg, $k = 1.0$, $M_\infty = 6.8$, $\alpha_0 = 0$ deg, and $h/L = 0.225$ for the Euler (– – –) and Navier–Stokes (——) calculations ($Re = 10^6$).

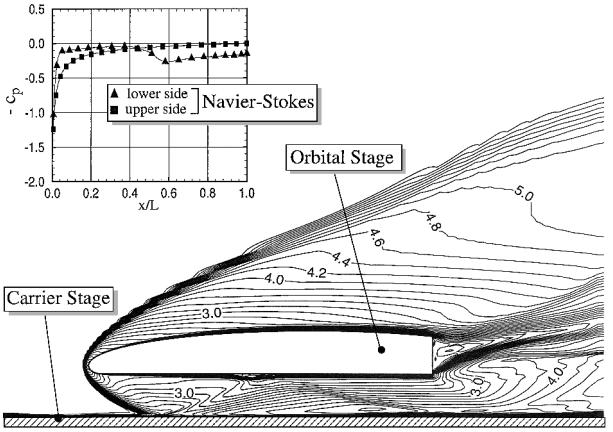

a) $h/L = 0.155$

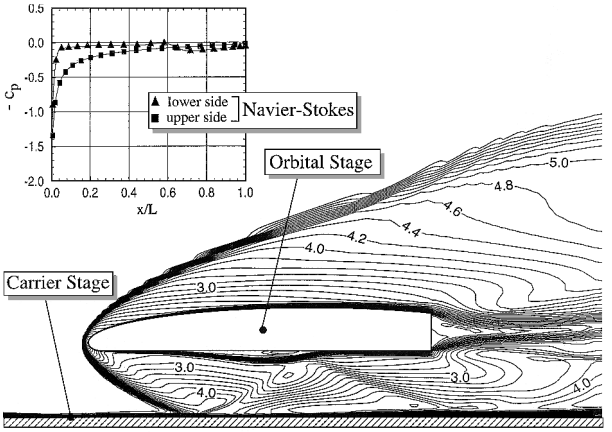

b) $h/L = 0.225$

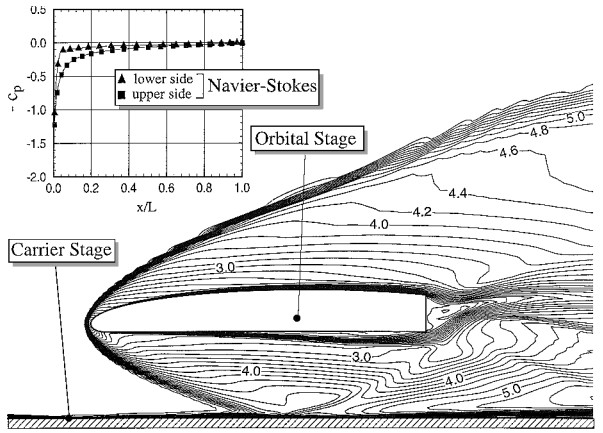

c) $h/L = 0.295$

Fig. 11 Mach number contours with $\Delta M/M_\infty = 0.1$ and surface pressure distribution of the translatory motion with amplitude $\Delta z/L = 0.07$, $k = 1.0$, $M_\infty = 6.8$, $Re = 10^6$, and $\alpha = 0$ deg obtained by the Navier–Stokes calculation.

unsteady results are compared (Figs. 5b and 11b). In comparison to the steady case (Fig. 5b), for the moving body, the area of separated flow occurs in the middle part of the orbital stage (Fig. 11b). Moreover, during liftoff the region of separated flow is smaller. Also, the shock wave reflected from the carrier stage hits the lower side of the orbital stage in the middle part (Fig. 11b) that results in a discontinous change of the c_p distribution. Consequently, in comparison to the steady state, the reflected shock wave system is shifted upstream in the unsteady case. This shift is caused by the motion-induced vertical velocity that results in a decrease of the pitch angle. In addition, the displacement of the expansion system upward is reduced in the unsteady case.

The steady and unsteady airloads resulting from the Euler and Navier–Stokes calculations are shown in Fig. 12. From the initial position, the orbital stage lifts off and reaches the upper turning point and then moves downward. Hereafter, the orbital vehicle passes the closest distance to the carrier stage, then it reaches the initial position again. During the upward movement the Navier–Stokes results show a zone of separated flow on the lower side of the orbital stage that is shifted from $x/L \approx 0.5$ to ≈ 0.65 (Figs. 11a–11c). Moving downward, this zone decreases and finally disappears at $h/L \approx 0.225$. During this phase, no shock wave reflections occur on the lower side of the orbital stage. At $h/L \approx 0.190$, a sudden increase of the lift and decrease of the moment coefficient can be detected for both

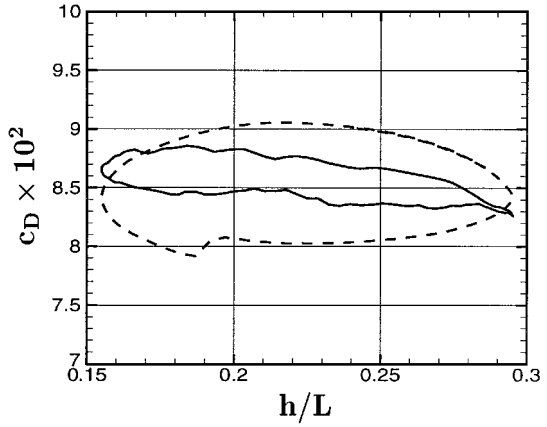

Drag coefficient $c_D(h/L)$

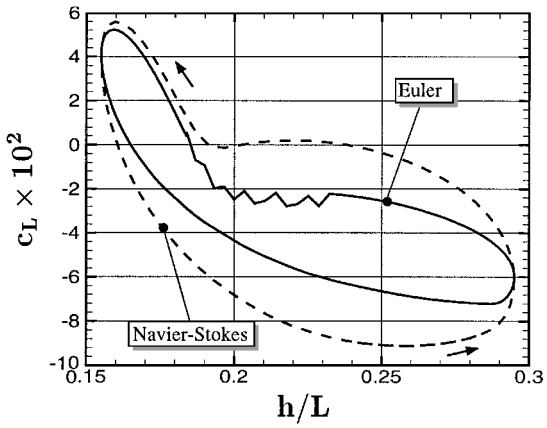

Lift coefficient $c_L(h/L)$

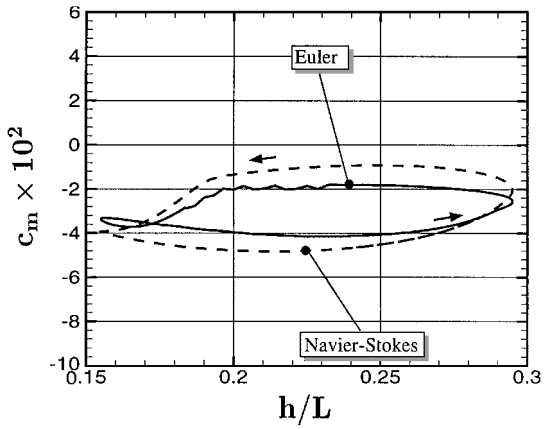

Pitch moment coefficient $c_m(h/L)$

Fig. 12 Aerodynamic coefficients of the translatory motion with amplitude $\Delta z/L = 0.07$, $k = 1.0$, $M_\infty = 6.8$, and $\alpha = 0$ deg for the Euler (——) and Navier–Stokes (– – –) calculations ($Re = 10^6$).

the Euler and Navier–Stokes results. This significant change in lift and moment coefficients is mainly caused by the complex shock wave system that is formed during the motion reflected from the carrier stage.

Conclusions

Steady and unsteady Euler and Navier–Stokes calculations have been performed for an idealized two-stage hypersonic vehicle. The influence of a harmonic pitching oscillation as well as of a translatory movement of the orbital stage on both the entire flowfield and the resulting airloads is investigated. The results obtained for both the Euler and Navier–Stokes studies indicate the same key features for the overall flowfield and result in aerodynamic coefficients of comparable magnitude. Nevertheless, differences between inviscid and viscous calculations are obvious concerning the intensity and interaction of the reflected shock wave system impinging on the orbital stage. The Navier–Stokes results reveal a zone of separated flow on the lower side of the orbital stage affecting the surface pressure distribution: Compared to the Euler calculations the discontinuity in surface pressure induced by the impinging shock wave is notably reduced while the impinging point is shifted downstream. The consequence is a slight decrease of the lift coefficient, especially for the pitching oscillation. In addition, the reduced lift force results in a reduced negative pitching moment with respect to the Euler calculations. Also, the expansion system in the wake region differs between Euler and Navier–Stokes results, leading to a higher pressure drag in the inviscid case. For the Euler calculations the harmonic components of the surface pressure show considerable values up to the third harmonic, whereas the Navier–Stokes results provide a stronger damping behavior. The zone of separated flow on the lower side of the orbital stage changes its shape and location during the motion. In connection with the displacement of the shock impinging point due to the motion-induced velocities, the unsteady effects significantly influence the airloads. Because the balance of moments is necessary for a safe and successful separation maneuver, the unsteady aerodynamic coefficients are essential for the prediction and have to be considered.

Acknowledgment

The work was carried out within the Collaborative Research Center 255 "Transatmospheric Flight Systems—Fundamentals of Aerothermodynamics, Powerplants and Flight Mechanics" of the German Research Association, Deutsche Forschungsgemeinschaft.

References

[1]Falempin, F., Scherrer, D., Laruelle, G., Rostand, P., Hermant, E., and Dubois, I., "French Hypersonic Propulsion Program PREPHA: Results, Lessons and Perspectives," AIAA Paper 98-1565, April 1998.

[2]Hirschel, E. H., "The Technology Development and Verification Concept of the German Hypersonics Programme," *Aerothermodynamics and Propulsion Integration for Hypersonic Vehicles*, R-813, AGARD, 1996, pp. 12-1–12-15.

[3]Maita, M., and Kubota, H., "Japanese Spaceplane/RLV Program," *AIAA 8th International Aerospace Planes and Hypersonic Systems and Technologies Conference*, AIAA, Reston, VA, 1998, pp. 1–9.

[4]Freeman, D., Reubusch, D., McClinton, C., Rausch, V., and Crawford, L., "The NASA Hyper-X Program," *Proceedings of the 48th International Astronautical Congress*, 1997.

[5]Kuczera, H., Hauck, H., Krammer, P., and Sacher, P. W., "The German Hypersonics Technology Programme—Status 1993 and Perspectives," AIAA Paper 93-5159, Nov. 1993.

[6]Hirschel, E. H., and Kuczera, H., "The FESTIP Technology Development and Verification Plan," AIAA Paper 98-1567, April 1998.

[7]Wilhite, A. W., "Analysis of Separation of Space Shuttle Orbiter from a Large Transport Airplane," NASA TM X-3492, June 1977.

[8]Weiland, C., "Stage Separation Aerodynamics," *Aerothermodynamics and Propulsion Integration for Hypersonic Vehicles*, R-813, AGARD, 1996, pp. 11-1–11-28.

[9]Bernot, P. T., "Abort Separation Study of a Shuttle Orbiter and External Tank at Hypersonic Speed," NASA TM X-3212, May 1975.

[10]Decker, J. P., and Gera, J., "An Exploratory Study of Parallel Stage Separation of Reusable Launch Vehicles," NASA TN D-4765, Oct. 1968.

[11]Naftel, J. C., Wilhite, A. W., and Cruz, C. I., "Analysis of Separation of a Two-Stage Winged Launch Vehicle," AIAA Paper 86-0195, Jan. 1986.

[12]Cvrlje, T., Breitsamter, C., Heller, M., and Sachs, G., "Unsteady Aerodynamics and Dynamic Stability of Hypersonic Flight Vehicles," *Jahrbuch des Deutschen Luft- und Raumfahrtkongresses/DGLR-Jahrestagung*, Vol. 1, Deutsche Gesellschaft für Luft- und Raumfahrt–Lilienthal–Oberth e.V. (DGLR), Bonn, 1998, pp. 89–102 (in German).

[13]Cvrlje, T., Breitsamter, C., and Laschka, B., "Unsteady Hypersonic Flows," Collaborative Research Center 255, Work and Result Rept. June 1995–June 1998, Technical Univ. of Munich, Garching, Germany, May 1998, pp. 21–89 (in German).

[14]Cvrlje, T., Breitsamter, C., Heller, M., and Sachs, G., "Lateral Unsteady Aerodynamics and Dynamic Stability Effects in Hypersonic Flight," *Proceedings of the International Conference on Methods of Aerophysical Research*, Pt. 1, Inst. of Theoretical and Applied Mechanics, Novosibirsk, Russia, 1998, pp. 44–54.

[15]Rochholz, H., "Eulerlösungen für den Separationsvorgang von Träger/Orbiter-Systemen im Hyperschall," Dr.-Ing. Dissertation, Technical Univ. of Munich, Garching, Germany, Aug. 1994.

[16]Rochholz, H., Huber, T., and Matyas, F., "Unsteady Airloads During the

Separation of an Idealized Two-Stage Hypersonic Vehicle," *Zeitschrift für Flugwissenschaften und Weltraumforschung*, Vol. 19, No. 1, 1995, pp. 2–9.

[17]Sonar, T., "Grid Generation Using Elliptic Partial Differential Equations," Deutsches Zentrum für Luft- und Raumfahrt, Inst. für Entwurfsaerodynamik, DFVLR, FB 89–15, Braunschweig, Germany, March 1989.

[18]Heller, G., "Aerodynamik von Deltaflügelkonfigurationen bei Schieben und Gieren," Dr.-Ing. Dissertation, Technical Univ. of Munich, Garching, Germany, July 1997.

[19]Anderson, D. A., Tannehill, J. C., and Pletcher, R. H., *Computational Fluid Dynamics and Heat Transfer*, 1st ed., McGraw–Hill, New York, 1984, pp. 479–482.

[20]Yee, H. C., "Upwind and Symmetric Shock-Capturing Schemes," NASA TM-89464, May 1987.

[21]Chakravarthy, S. R., and Osher, S., "High-Resolution Applications of the Osher Upwind Scheme for the Euler Equations," AIAA Paper 83-1943, July 1983.

[22]Chakravarthy, S. R., "High–Resolution Upwind Formulations for the Navier–Stokes Equations," von Karman Inst. Lecture Series on Computational Fluid Dynamics, VKI 1988-05, 1988, pp. 1–105.

[23]Holden, M. S., and Moselle, J. R., "Theoretical and Experimental Studies of the Shock Wave–Boundary Layer Interaction on Compression Surfaces in Hypersonic Flow," ARL 70-0002, Jan. 1970; also Calspan, Rept. AF-2410-A-1, Buffalo, NY, Oct. 1969.

[24]Blazek, J., "Investigations of the Implicit LU-SSOR Scheme," Deutsches Zentrum für Luft- und Raumfahrt, Inst. für Entwurfsaerodynamik, DLR, FB 93-51, Braunschweig, Germany, July 1993.

[25]Leyland, P., Richter, R., and Neve, T., "High Speed Flows over Compression Ramps," *Proceedings of the Ninth GAMM-Conference on Numerical Methods in Fluid Mechanics*, Vol. 35, Notes on Numerical Fluid Mechanics, Vieweg, Braunschweig, Germany, 1992, pp. 223–236.

[26]Schoder, W., and Rochholz, H., "Separation of Two-Stage Hypersonic Vehicles," *2nd Space Course on Low Earth Orbit Transportation*, Vol. 1, Technical Univ. of Munich, Munich, Germany, Oct. 1993, pp. 36-1–36-22.

J. R. Maus
Associate Editor